minerals

MDPI

Article

Glauconite-Based Nanocomposites with Zn/Cu/B: Multifunctional Micronutrient Fertilizers

Ivan Khitrin [1], Prokopiy Maximov [1], Evan Dasi [1], Kanipa Ibraeva [2], Konstantin Ponomarev [2], Natalia Maximova [1], Peter Belousov [3], Alexey Ruban [1] and Maxim Rudmin [1,*]

[1] Division for Geology, School of Earth Sciences & Engineering, Tomsk Polytechnic University, 634050 Tomsk, Russia; ish9@tpu.ru (I.K.); pnm1@tpu.ru (P.M.); de01@tpu.ru (E.D.); nak58@tpu.ru (N.M.); ruban@tpu.ru (A.R.)
[2] Institute of Environmental and Agricultural Biology (X-BIO), University of Tyumen, 625003 Tyumen, Russia; k.ibraeva@utmn.ru (K.I.); k.o.ponomarev@utmn.ru (K.P.)
[3] Institute of Geology of Ore Deposits, Petrography, Mineralogy and Geochemistry, Russian Academy of Science (IGEM RAS), 119017 Moscow, Russia; belousov.peter@list.ru
* Correspondence: rudminma@tpu.ru

Abstract: The full potential of glauconite-based nanocomposites as micronutrient fertilizers remains underexplored, particularly their interaction with Zn, Cu, and B. Despite the promising applications, the mechanisms of nutrient sorption and their effects on plant growth require further investigation, especially concerning structural changes and nutrient delivery efficiency. This study investigates the modification of glauconite with Zn, Cu, and B solutions to create multifunctional nanocomposites with enhanced properties. It was established that the activation process preserves the primary globular–lamellar morphology of glauconite while introducing structural changes. Nanocomposites were synthesized using chemical activation and characterized using XRD, SEM-EDS, TEM, FTIR, and BET analyses. Agrochemical tests evaluated their effects on oat growth under controlled conditions. Nanocomposites with zinc sulfate exhibited an increase in specific surface area and mesoporosity, enhancing sorption capacity and facilitating the formation of inner-sphere complexes on the mineral's basal surface. Modification with copper led to the formation of secondary phases, such as sulfates, on the surfaces of microflakes and globules while preserving the crystalline structure with inner-sphere coordination of Cu^{2+}. Boron-modified nanocomposites were characterized by localized restructuring, pore channeling, and an increase in mesopore diameter, along with the formation of outer-sphere complexes relative to the basal surface of glauconite. Thermogravimetric and calorimetric analyses with mass spectrometry revealed specific endothermic and exothermic effects, particularly in Zn-modified samples, confirming changes in dehydration energetics. Agricultural tests on oats (*Avena sativa*) demonstrated the effectiveness of Cu- and B-modified nanocomposites in improving plant growth parameters, including a 7% increase in plant height and a 6.4% increase in dry weight. Zn-modified nanocomposites showed high germination rates (up to 100%) at low dosages but require optimization to avoid phytotoxicity at higher concentrations. The findings highlight the potential of adapting nanocomposites for targeted nutrient release. Additionally, glauconite nanocomposites have potential applications in restoring degraded soils, treating polluted runoff, and developing slow-release agrochemical systems.

Keywords: chemical activation; glauconite; globules; micronutrients; potassium; slow-release fertilizer

Academic Editors: Davide Lenaz, Filippo Parisi and Andrey G. Kalinichev

Received: 16 November 2024
Revised: 23 December 2024
Accepted: 25 December 2024
Published: 26 December 2024

Citation: Khitrin, I.; Maximov, P.; Dasi, E.; Ibraeva, K.; Ponomarev, K.; Maximova, N.; Belousov, P.; Ruban, A.; Rudmin, M. Glauconite-Based Nanocomposites with Zn/Cu/B: Multifunctional Micronutrient Fertilizers. *Minerals* **2025**, *15*, 12. https://doi.org/10.3390/min15010012

1. Introduction

Multifunctional fertilizers (controlled-release or slow-release fertilizers) are a key focus in the development of sustainable agriculture. They aim to solve two primary challenges: providing plants with nutrients while minimizing losses and reducing the negative environmental impact [1–4]. Unlike traditional fertilizers, which are prone to rapid leaching and result in excessive nutrient accumulation in soil and water systems, multifunctional fertilizers (or smart fertilizers) enable targeted nutrient delivery with a prolonged effect [5–7].

Excessive use of fertilizers in conventional systems leads to several environmental problems, including denitrification, increased greenhouse gas emissions, eutrophication of water bodies, and soil quality degradation [8–11]. In the context of global population growth and the need to enhance food security, these issues necessitate adopting innovative approaches, such as environmentally safe and resource-efficient technologies, among which multifunctional fertilizers play a prominent role [12–14].

Modern synthesis schemes for multifunctional fertilizers involve various methods [15–17] that enable the modification of the physicochemical properties of carriers (or inhibitors). The primary function of these systems is to create matrices that can retain and slowly release nutrients. Critical materials for such multifunctional fertilizers include polymeric, organo-polymeric, organo-mineral, and mineral substances [18–20]. Natural layered silicates, such as smectites, kaolinite, vermiculite, and glauconite, are particularly noteworthy [21,22]. These materials possess unique structures and properties, including high ion exchange capacity, stability, and eco-safety.

Due to its chemical composition and structural characteristics, glauconite is particularly interesting for agricultural applications [17,21]. It is a dioctahedral, potassium-rich, iron-bearing 2:1 phyllosilicate mica with interlayer deficiency [23–29]. Its natural globular morphology [30,31] and ion exchange properties enhance nutrient availability [32].

Previous studies have demonstrated the potential of glauconite as a source of macro- and micronutrients due to its unique crystal structure, which allows for gradual nutrient release. For instance, some researchers [33,34] reported the effectiveness of chemically activated glauconite in improving soil fertility and plant growth under controlled conditions. Similarly, Rudmin et al. [32] highlighted the potential of nanocomposite-based fertilizers derived from glauconite for controlled nutrient release, showing enhanced agricultural performance. However, while significant progress has been made, the specific mechanisms governing the sorption and controlled release of micronutrients such as Zn, Cu, and B remain insufficiently studied, particularly in relation to their structural modifications and thermal stability.

Building upon previous findings, we hypothesize that chemical activation of glauconite with micronutrients such as Zn, Cu, and B leads to the formation of nanocomposites with enhanced sorption properties and controlled nutrient release. In this study, the term ”multifunctional fertilizers” is used as an overarching concept encompassing controlled-release fertilizers (CRFs) and slow-release fertilizers (SRFs), along with additional functional benefits, such as enhancing soil water retention and providing potassium as a macronutrient.

The study investigates the detailed interaction of micronutrients (Zn, Cu, and B) with glauconite to create multifunctional and composite nanocomposites with globular morphology. The research involves stepwise and detailed modifications of mineral-to-solution ratios to evaluate the sorption factors of the introduced ions in the macro-, meso-, micro-, and nanopores of glauconite.

2. Materials and Methods

2.1. Mineral Material

Glauconite from the Karin deposit (Chelyabinsk region, Russia) was selected for this study due to its high purity and unique composition. The glauconite concentrate was prepared via the following steps: (i) removal of the clay fraction by decantation in distilled water, (ii) electromagnetic separation, and (iii) manual refinement of the magnetic fraction. The clay fraction was removed from the mineral material, and a concentrate of globular glauconite was used for further processing. This step facilitates the exposure of internal sorption sites and optimizes surface reactivity for subsequent chemical treatment.

The final concentrate contained approximately 95% globular glauconite, with minor impurities of quartz and feldspar (~5%). The chemical composition of the initial glauconite, determined via energy-dispersive analysis, included 6.8–9.4 wt.% K_2O, 18.1–32.9 wt.% $Fe_2O_{3(total)}$, 50.2–58.2 wt.% SiO_2, 3.8–11.8 wt.% Al_2O_3, 2.9–4.7 wt.% MgO, 0.4–0.6 wt.% CaO, 0.3–0.4 wt.% Na_2O and 1.7–4.5 wt.% LOI (loss on ignition). The structural formula of glauconite was determined as $K_{0.6–0.8}(Al_{0.2–0.7}Mg_{0.3–0.5}Fe_{0.9–1.7})_{1.6–2.0}(Si_{3.5–3.8}Al_{0.2–0.6})O_{10}(OH)_2nH_2O$.

2.2. Preparation of Nanocomposites

The nanocomposites were prepared through the chemical interaction of globular glauconite concentrate with various solutions. Solutions containing micronutrients were prepared by dissolving 0.15, 0.3, and 0.6 g of different substances (zinc sulfate, copper chelate, and boric acid) in 30 mL of distilled water, corresponding to 5, 10, and 20 g/L. Subsequently, the nine solutions were added to globular glauconite concentrates (50 g) and mixed in Petri dishes. The absorption process continued for 48–72 h until the mixture reached a dry consistency. The preparation method for Zn-, Cu-, and B-modified nanocomposites follows established protocols [32], ensuring reproducibility and quality control of materials.

As a result, nine sediment samples were obtained and named as follows:

- Gk3Zn2-05, Gk3Zn2-10, Gk3Zn2-20 for zinc sulfate solutions at concentrations of 5 g/L, 10 g/L, and 20 g/L, respectively;
- Gk3Cu2-05, Gk3Cu2-10, Gk3Cu2-20 for copper chelate solutions at concentrations of 5 g/L, 10 g/L, and 20 g/L, respectively;
- Gk3B2-05, Gk3B2-10, Gk3B2-20 for boric acid solutions at concentrations of 5 g/L, 10 g/L, and 20 g/L, respectively.

2.3. Characterization of Nanocomposites

The synthesized nanocomposites were analyzed using a variety of techniques, including X-ray diffraction (XRD), scanning electron microscopy coupled with energy-dispersive X-ray spectroscopy (SEM-EDS), transmission electron microscopy (TEM) with selected area electron diffraction (SAED), Fourier transform infrared spectroscopy (FTIR), thermal analysis methods such as thermogravimetric analysis and differential scanning calorimetry integrated with a quadrupole mass spectrometer (TG-DSC-MS), inductively coupled plasma mass spectrometry (ICP-MS), and the Brunauer–Emmett–Teller (BET) method.

Structural changes in nanocomposites were investigated in randomly oriented samples using a Bruker D2 Phase X-ray diffractometer (Billerica, MA, USA) equipped with Cu-Kα radiation, operating at 10 mA and 30 kV. Composite fractions smaller than 10 μm were scanned over a 2θ range of 4° to 50°, with a step size of 0.02°, a scanning rate of 1.5 s per step, a divergence slit of 1 mm, an anti-scatter slit of 3 mm, and a receiving slit of 0.3 mm. The quantitative mineralogical composition of the entire sample was determined using Rietveld analysis with PDXL and Siroquant 3.0 software.

Nanocomposite crystal unit structure and interlayer spaces were investigated using a JEOL JEM-2100F transmission electron microscope (TEM) at the "Nanomaterials and Nanotechnologies" lab at the Tomsk Polytechnic University. A drop of the nanocomposite suspension was deposited onto a carbon-coated copper grid (300 mesh, 3.05 mm in diameter) and allowed to dry before analysis. Scanning was operated in transmission mode at an acceleration voltage of 200 kV, and images were captured from sufficiently thin regions of the sample.

The FTIR spectra of the nanocomposites were recorded in the range of 4000–400 cm^{-1} using a Shimadzu FTIR 8400S spectrometer (Kyoto, Japan) equipped with a temperature-controlled high-sensitivity DLATGS detector. The analysis was performed using KBr pellets with a spectral resolution of 4 cm^{-1} to identify the functional groups of chemical bonds present in the synthesized nanocomposites.

The element concentrations (ppm) in the nanocomposites were measured using inductively coupled plasma mass spectrometry (ICP-MS) on an ELAN DRC-e spectrometer. Approximately 0.5 g of powdered sample underwent a procedure with the following steps: (i) fusion at 1050 °C with 0.8 g of $LiBO_2/Li_2B_4O_7$ flux; (ii) dissolution in a mixture of HF, HNO_3, and $HClO_4$ (ratios 5:4:1.5) at 120 °C; (iii) evaporation at 160 °C; (iv) dissolution in 5M HNO_3; (v) filtration; and (vi) ICP-MS analysis [35]. Accuracy and precision were evaluated through repeated measurements of samples and standards.

Thermogravimetric and differential scanning calorimetry (TG-DSC) curves for the studied mineral substances were recorded over a temperature range of 30 to 1000 °C under an inert argon atmosphere (flow rate: 50 mL/min) with a heating rate of 10 °C/min. The measurements were performed using an STA 449 F5 Jupiter micro-thermal analyzer (NETZSCH, Selb, Germany) to determine the weight ratios of sorbent substances and analyze thermal degradation processes. The TG-DSC analysis was integrated with a Netzsch TA Quadrupole Mass Spectrometer (QMS) 403C Aeolos via a transfer line maintained at 250 °C, enabling simultaneous detection of evolved ions. Before experimentation, the system underwent comprehensive calibration, including the analyzer and buoyancy baseline adjustments. The mass spectrometer was operated in electron impact ionization mode, monitoring mass-to-charge (m/z) ratios from 1 to 50.

The morphology of nanocomposites was studied using a TESCAN VEGA 3 SBU scanning electron microscope (Brno, Czech Republic) equipped with an OXFORD X-Max 50 energy-dispersive spectrometer (High Wycombe, UK). The analysis was conducted at an accelerating voltage of 10–20 kV, a specimen current of 3–12 nA, and a spot diameter of approximately 2 μm.

The specific surface area of the samples was determined using the Brunauer–Emmett–Teller (BET) method with a 3P sync 210 specific surface and porosity analyzer (Ribori Instrumentation, Genay, France). Before analysis, the samples were dried at 125 °C for 2 h and then degassed under vacuum at 250 °C for 12 h. The surface area measurements were conducted at 196 °C within a relative pressure range of 0.05 to 0.3. The nitrogen adsorption–desorption isotherms also determined the average pore size and total pore volume.

2.4. Agricultural Tests with Nanocomposites

Laboratory agro-tests were conducted to evaluate the effects of glauconite-based nanocomposites on the growth of oats (*Avena sativa*). The experiments were conducted on grey podzolic soil (4.8% humus, pH 4.9) with fertilizer application at 0.5 t/ha (0.3 g per experimental unit/plot). The soil used in this study was classified as Haplic Chernozem according to the World Reference Base for Soil Resources (WRB). Its texture composition was 40% silt, 35% clay, and 25% sand, creating a balanced medium for plant growth experiments. The dosage was calculated based on the total glauconite mass rather than the micronutrient

content (9, 18, 36 mg Zn/Cu/B). Each experiment was conducted separately for one type of nanocomposite (with Zn, Cu, or B), ensuring that no combined treatments with different micronutrients were applied in the same plot. In addition to the nanocomposites, four additional experimental units were included using standard fertilizers, namely zinc sulfate, copper chelate, and boric acid, each prepared at a concentration of 20 mg Zn/Cu/B per experimental unit and glauconite at 0.3 g per experimental unit. These treatments were used as reference variants to compare the effects of traditional fertilizers with glauconite-based nanocomposites. This setup allowed us to evaluate the specific effects of each nanocomposite independently. The experimental design assessed the specific effects of Zn-, Cu-, and B-modified glauconite nanocomposites.

Each experimental block consisted of three replicates (units). Each unit contained 85 g of soil and 25 oat seeds. Experimental blocks included 14 variants: controls (without fertilizer, with zinc sulfate, copper chelate, boric acid, and glauconite) and 9 nanocomposites. Units were arranged randomly and repositioned weekly throughout the experiment to minimize environmental variability. Each pot had a capacity of approximately 150 mL, with soil moisture content maintained at ~70% of the total water-holding capacity to ensure optimal plant growth. Oat (*Avena sativa*) was selected for its agricultural relevance and high sensitivity to micronutrient availability. Seeds used in the experiments were sourced from certified agricultural suppliers to ensure seed quality and uniformity for controlled agro-tests. This selection allowed for a thorough evaluation of the fertilizers' efficacy in promoting early plant development. The experiment lasted 14 days. Under controlled conditions, germination energy and rate, plant height, and dry weight (biomass) were measured after fertilizer application. Statistical analysis was performed using Student's *t*-test ($p < 0.05$), and results were presented as arithmetic means with standard errors.

3. Results

3.1. Crystal Structure of Nanocomposites

The X-ray diffraction patterns of the nanocomposites indicate the stability of the glauconite crystalline lattice (10.0, 4.5, 2.6, 2.45, and 2.25 Å) after interaction with the reactive solutions (Figure 1). For all nanocomposites with maximum micronutrient concentrations (Gk3Zn2-20, Gk3Cu2-20, and Gk3B2-20), a slight shift in the basal peak of glauconite from 10.09 to 10.15 Å is observed. This suggests adsorption on the basal plane of the crystalline layers due to the inner-sphere coordination of zinc, copper, or boron ions.

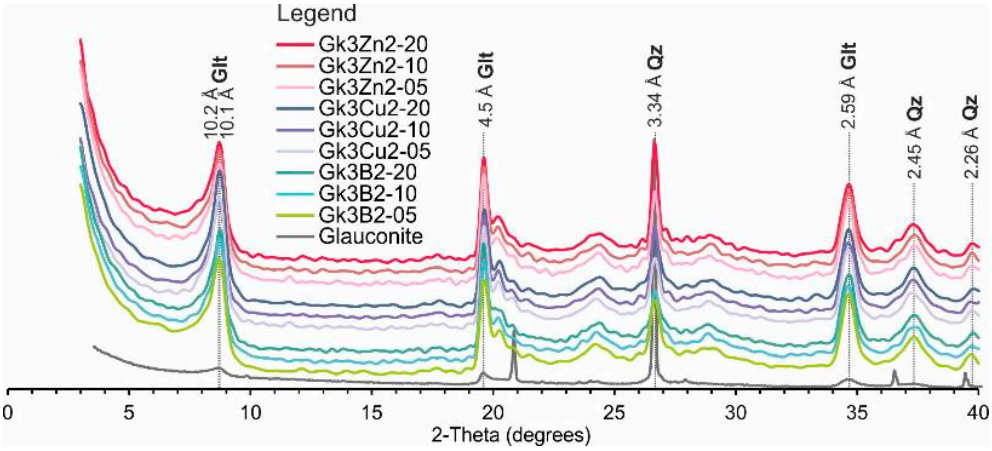

Figure 1. X-ray diffraction patterns of activated nanocomposites and the initial glauconite concentrate: Glt—glauconite, Qz—quartz.

High-resolution TEM and selected area electron diffraction (SAED) images (Figure 2) illustrate local changes in the unit structure of nanocomposite crystallites. The interlayer thickness varies depending on the type of modification: 1.5–2.2 Å for zinc-modified nanocomposites, 1.6–2.3 Å for copper-modified nanocomposites, and 1.4–3.1 Å for boron-modified nanocomposites. Boron-modified nanocomposites demonstrate the most significant expansion of the crystalline layers. In contrast, zinc-modified nanocomposites show minimal expansion, indicating that sorption processes predominantly occur in the micro- and nanopores of glauconite.

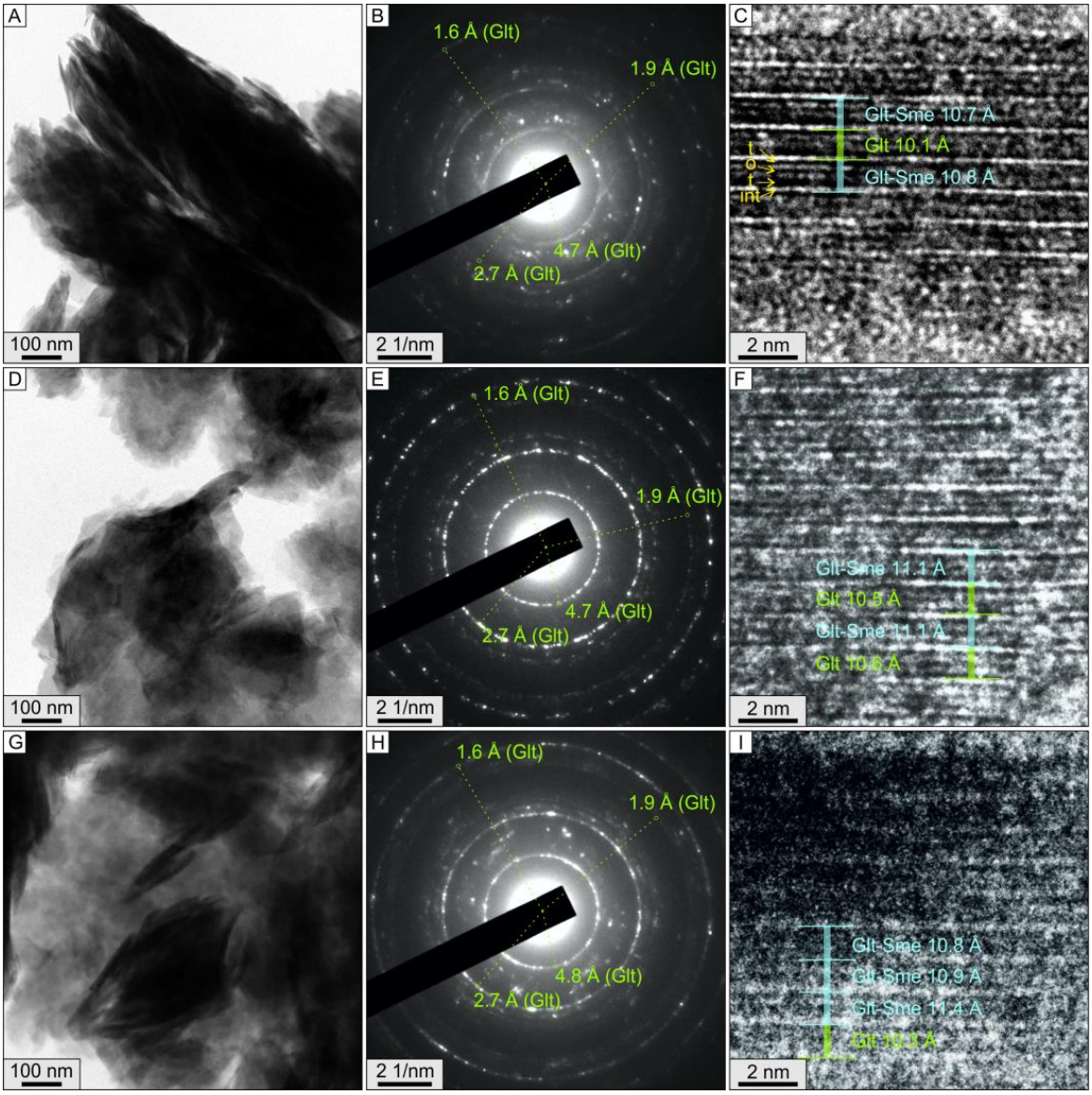

Figure 2. High-resolution TEM images (**A**,**C**,**D**,**F**,**G**,**I**) and SAED patterns (**B**,**E**,**H**) of activated nanocomposites: (**A**–**C**) Gk3Zn2-20and (**D**–**F**) Gk3B2-20. High-magnification TEM images (**D**,**F**,**I**) reveal structural changes in the smectite layers within the glauconite nanocomposite caused by interlayer expansion and modifications of the crystalline layers. Abbreviations: Glt—glauconite crystalline layers, Glt-Sme—smectite layers within glauconite, t—tetrahedral sheet, o—octahedral sheet, int—interlayer space.

The FTIR spectra of the nanocomposites confirm that the basic structure of glauconite remains intact after chemical treatment (Figure 3). All samples exhibit characteristic frequencies corresponding to the crystalline framework. In the low-frequency region, bands

at 430–500 cm^{-1} and 670–680 cm^{-1} are observed across all samples, indicating Al-O-Si and O-Si-O deformation vibrations. Additional specific bands were registered in this region: around 700 and 820 cm^{-1} for zinc-modified nanocomposites, 815 cm^{-1} for copper-modified nanocomposites, and ~817 cm^{-1} for boron-modified nanocomposites. In the mid-frequency region, the peak at 1010 cm^{-1} corresponds to Si-O stretching vibrations. A weak peak at 1115–1120 cm^{-1}, detected in zinc-modified nanocomposites, indicates localized structural changes. For boron-modified samples (Gk3B2-20), B-O stretching vibrations were identified at 1420 cm^{-1} in this region, suggesting boron incorporation via outer-sphere coordination. The high-frequency region reflects hydroxyl group vibrations in the ranges of 3400–3420 cm^{-1} and 3600–3650 cm^{-1}.

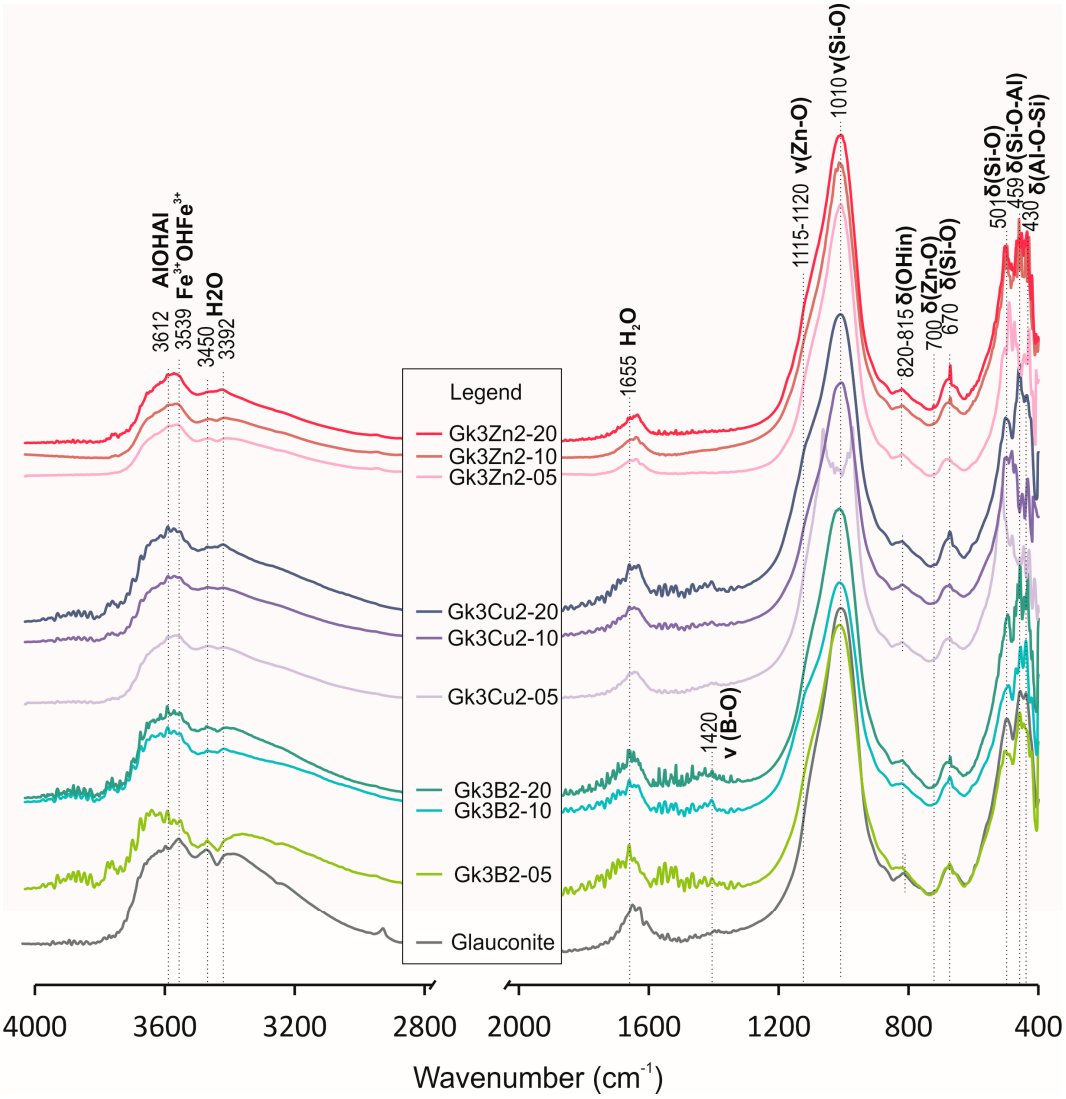

Figure 3. FTIR spectra of activated nanocomposites and the initial glauconite. Abbreviations: δ—deformation vibrations, ν—stretching vibrations.

A comparison of FTIR bands for nanocomposites with varying concentrations of Zn, Cu, and B revealed specific trends. For zinc-modified nanocomposites, the intensity of the 700 and 1120 cm^{-1} bands increased with higher Zn concentrations, suggesting more extensive interaction between Zn ions and the siloxane framework of glauconite. Copper-modified nanocomposites exhibited a consistent 815 cm^{-1} band across concentrations, indicating stable Cu-O bonding irrespective of concentration. In boron-modified nanocomposites, the 1420 cm^{-1} peak corresponding to B-O stretching vibrations became more

pronounced at higher B concentrations, indicating enhanced outer-sphere coordination or the basal edge.

3.2. Nanocomposites' Composition

The composition of major oxides in glauconite nanocomposites shows minimal differences compared to the original material, confirming the stability of the mineral structure. However, key micronutrient concentrations change significantly due to the adsorption of target ions (Table 1). Zinc content increased from 0.17% in Gk3Zn2-05 to 0.64% in Gk3Zn2-20, confirming the sorption of Zn^{2+} ions in the micro- and nanopores of glauconite. SEM-EDS analysis revealed localized Zn enrichment of up to 1 wt.% in the near-surface regions of glauconite grains in Gk3Zn2-20 (Figure 4). A similar trend was observed for copper, with Cu content increasing from 256 to 893 ppm in samples modified with copper chelate (Table 1) as the concentration of the reacting solution increased. Potassium content remained stable, indicating the involvement of interlayer water in sorption processes and ruling out potassium substitution.

Table 1. Bulk chemical composition of nanocomposites according to ICP-MS analysis.

Samples	Na (%)	Mg (%)	Al (%)	K (%)	Ca (%)	Ti (%)	Mn (%)	Fe (%)	Cu (ppm)	Zn (ppm)
Gk3Zn2-20	0.07	2.7	5.0	6.9	0.028	0.10	0.014	18.2		6363
Gk3Zn2-10	0.06	2.7	4.8	6.7	0.029	0.09	0.015	17.7		3510
Gk3Zn2-05	0.06	2.5	4.5	6.5	0.027	0.11	0.014	17.0		1754
Gk3Cu2-20	0.16	2.8	5.1	7.0	0.028	0.08	0.014	18.1	893	125
Gk3Cu2-10	0.11	2.7	4.9	6.8	0.027	0.08	0.014	17.8	415	126
Gk3Cu2-05	0.09	2.7	5.0	6.9	0.028	0.09	0.014	18.2	256	142
Gk3B2-20	0.07	2.7	4.9	6.7	0.028	0.08	0.014	17.5		122
Gk3B2-10	0.07	2.7	4.9	6.8	0.028	0.07	0.014	17.8		122
Gk3B2-05	0.07	2.7	5.1	7.0	0.029	0.07	0.012	17.9		123

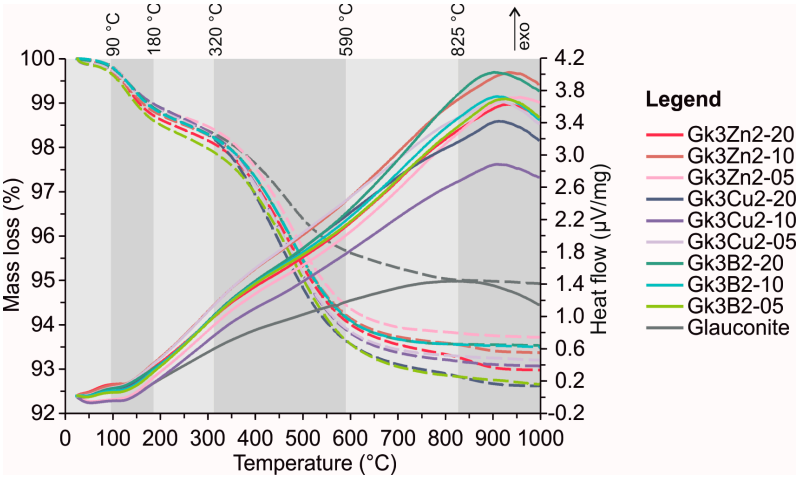

Figure 4. TG (dashed lines) and DSC curves (solid lines) of prepared nanocomposites and original glauconite.

For all nanocomposites, the DSC curves (Figure 4) exhibit two endothermic effects at 55 °C and 130 °C and one exothermic effect at 85 °C (Table 2), associated with the removal of physically bound water and slight oxidation of iron in the octahedral positions of glauconite. The exothermic effect at 900–940 °C shows distinctive features: it occurs at 900–910 °C in B-modified nanocomposites, at 920–930 °C in Cu-modified nanocomposites, and at 945–950 °C in Zn-modified nanocomposites. This exothermic effect is nearly absent in the original glauconite, with a weak broad peak at ~850 °C. These results confirm that the modification of glauconite with Zn, Cu, and B alters the amorphization.

Table 2. Weight losses, thermic effects, and released ions of glauconite-based nanocomposites and glauconite according to TG-DSC-MS analysis.

	Nanocomposites	Weight Loss Intervals (°C)					
		0–90	**90–180**	**180–320**	**320–590**	**590–825**	**825–1000**
Weight loss (%)	Gk3Zn2-05	99.9	99.0	98.4	94.4	93.8	93.7
	Gk3Zn2-10	99.8	98.9	98.2	94.2	93.6	93.4
	Gk3Zn2-20	99.8	98.8	98.0	94.1	93.3	93.0
	Gk3Cu2-05	99.8	99.0	98.2	93.9	93.3	93.2
	Gk3Cu2-10	99.8	99.0	98.2	93.9	93.2	93.1
	Gk3Cu2-20	99.8	99.0	98.1	93.6	92.8	92.6
	Gk3B2-05	99.7	98.6	97.8	93.6	92.8	92.7
	Gk3B2-10	99.9	98.9	98.2	94.2	93.6	93.5
	Gk3B2-20	99.8	98.9	98.2	94.2	93.6	93.5
	Glauconite	99.9	99.0	98.3	95.7	95.0	94.9
Final residue (%)	Gk3Zn2-05	0.14	0.89	0.61	3.91	0.63	0.10
	Gk3Zn2-10	0.24	0.91	0.69	3.94	0.67	0.19
	Gk3Zn2-20	0.18	1.06	0.72	3.95	0.82	0.29
	Gk3Cu2-05	0.21	0.84	0.78	4.25	0.63	0.10
	Gk3Cu2-10	0.21	0.77	0.80	4.33	0.71	0.11
	Gk3Cu2-20	0.19	0.79	0.89	4.48	0.81	0.21
	Gk3B2-05	0.29	1.07	0.80	4.19	0.82	0.18
	Gk3B2-10	0.14	0.95	0.75	3.98	0.63	0.06
	Gk3B2-20	0.16	0.90	0.76	4.02	0.60	0.04
	Glauconite	0.13	0.89	0.71	2.61	0.65	0.08
Thermic effects (°C) *	Gk3Zn2-05	↓55 and ↑85	↓130				
	Gk3Zn2-10						↑945–950
	Gk3Zn2-20						
	Gk3Cu2-05						
	Gk3Cu2-10						↑920–930
	Gk3Cu2-20						
	Gk3B2-05						
	Gk3B2-10						↑900–910
	Gk3B2-20						
	Glauconite						↑850
Detected ions (*m*/*z*)	Gk3Zn2-05	17, 18	16–18	16	16–18	12, 44	24, 48, 50
	Gk3Zn2-10	17, 18	16–18	16, 30	16–18, 30	12, 22, 30, 44	24, 48, 50
	Gk3Zn2-20	17, 18	16–18	16, 30	16–18, 30	12, 22, 30, 44	24, 48, 50
	Gk3Cu2-05	18	16–18		17–18, 30		48
	Gk3Cu2-10	18	16–18	16, 30, 44	12, 17–18, 30, 44	12, 44	48
	Gk3Cu2-20	18	16–18, 22	16, 30, 44	12, 17–18, 22, 30, 44	12, 22, 44	24, 48, 50
	Gk3B2-05		16–18		18		
	Gk3B2-10	17–18	16–18		16–18, 30	12, 30, 44	
	Gk3B2-20		16–18		17–18, 30	30, 44	
	Glauconite		16–18		16–18	44	

* Note: ↓—endothermic effects, ↑—exothermic effects.

The thermogravimetric (TG) curves reveal 5–6 weight loss intervals (Figure 4). Six intervals are characteristic only for Zn-modified nanocomposites. The original glauconite and nanocomposites with Cu and B exhibit five weight loss intervals: 0–90, 90–180, 180–320, 320–590, and 590–1000 °C:

0–90 °C: removal of physically bound water, accounting for 0.1–0.3 wt.%;

90–180 °C: desorption of water (OH^+, H_2O) and, in Zn-modified nanocomposites, water from the macroporous spaces, amounting to 0.8–1.1 wt.%;

180–320 °C: release of mesoporous water (OH^+, H_2O) in minor amounts, along with ions from the decomposition of organic impurities (C^+) in the original glauconite and chelates or sulfates (O^+, NO^+, CO_2^+), contributing to 2.1–10.6 wt.% (Figure 5);

320–590 °C: removal of water (OH^+, H_2O) and decomposition products (C^+, NO^+, and CO_2^+), predominantly from the interlayer space, resulting in 3.9–4.5 wt.% weight loss;

590–1000 °C: dehydration of the glauconite crystal lattice, contributing 0.6–1.1 wt.% of weight loss, releasing C^+, NO^+, and CO_2^+ ions. In this interval, SO^+ release is distinctly

observed between 825 and 1000 °C in Zn-sulfate-modified nanocomposites, accounting for an additional 0.1–0.3 wt.% weight loss due to further layer lattice dehydration.

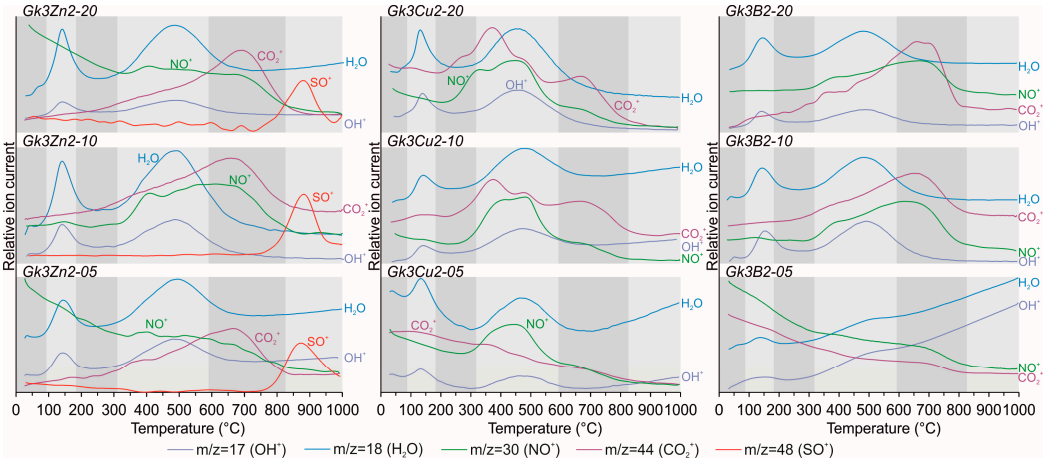

Figure 5. Selected representative curves for studied nanocomposites from mass spectrometry (MS) multi-ion detection are showcased, specifically for ions with mass-to-charge ratios (m/z) of 17 (OH^+), 18 (H_2O), 30 (NO^+), 42 (NCO^+), 44 ($CO_2{}^+$), and ($SO_3{}^+$).

3.3. Morphology of Nanocomposites

Modifying glauconite with Zn, Cu, and B solutions preserves its primary globular flaky morphology while inducing some changes (Figure 6). The size of nanocomposite microparticles ranges from 9 to 15 µm. Zn-modified nanocomposites retain the globular structure with mesopores ranging from 10 to 50 nm in diameter. In Cu-modified nanocomposites, small particles measuring 100–500 nm are observed on the surface of microparticles or globules due to the formation of secondary phases, such as sulfates. The most pronounced morphological changes are seen in B-modified nanocomposites, where a highly porous structure with mesopore diameters of 20–70 nm is formed, accompanied by the channeling and localized rearrangements of microparticles (Figure 6). The sorption of $BO_3{}^-$ and $BO_4{}^-$ groups leads to changes in the average pore size, the loosening of microparticles, and a reduction in their tortuosity. The morphological features, combined with chemical composition, highlight glauconite's dual role as a nutrient container and a nutrient source. This unique sorption behavior at basal surfaces and edges reflects its multifunctional potential in advanced fertilizer design.

The initial globular glauconite exhibits a specific surface area of 41.2 m^2/g, a pore volume of 0.06 cm^3/g, and an average pore size of 5.4 nm (Table 3). Activation of glauconite with zinc sulfate, copper chelate, and boric acid solutions has different effects on its specific surface area and porosity. Nanocomposites treated with zinc sulfate solutions significantly increase in specific surface area (from 46.9 m^2/g to 50.0 m^2/g) and pore volume, attributed to forming a new phase (sulfates). Activation with copper chelate maintains a nearly unchanged specific surface area (46.0–47.7 m^2/g), indicating the stabilization of the globular-layered structure of glauconite without substantial changes in porosity. In contrast, boric acid treatment decreases the specific surface area (45.6 m^2/g to 36.3 m^2/g) and increases the mesopore diameter from 5.4 nm in the initial glauconite to 7.4 nm in Gk3B2-20. Due to pore filling and changes in their morphological structure, it manifests as the loosening of microparticles and a reduction in their tortuosity (Figure 6).

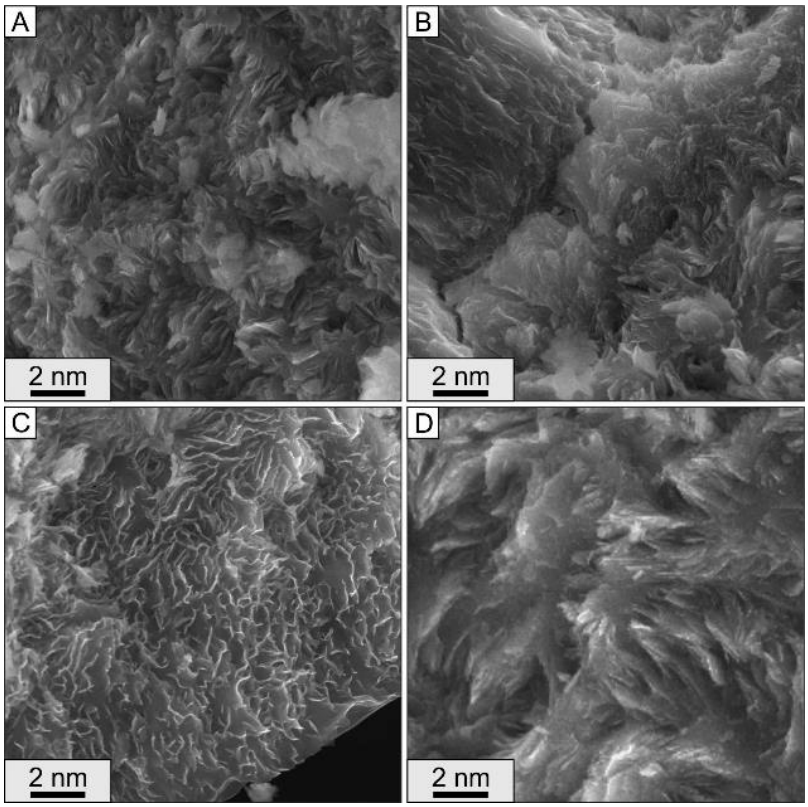

Figure 6. SEM images in a secondary electron detector showing different morphological features of the nanocomposites: (**A**) Gk3Zn2-20, (**B**) Gk3Cu2-20, (**C**) Gk3B2-20, and (**D**) original glauconite.

Table 3. Specific surface area, total pore volume, and average pore diameter of nanocomposites according to BET analysis.

Nanocomposites	Specific Surface Area (m^2/g)	Total Pore Volume (cm^3/g)	Average Pore Diameter (nm)
Gk3Zn2-05	46.9	0.070	6.0
Gk3Zn2-10	48.1	0.068	5.7
Gk3Zn2-20	50.0	0.077	6.1
Gk3Cu2-05	47.7	0.071	5.9
Gk3Cu2-10	46.1	0.069	6.0
Gk3Cu2-20	46.0	0.069	6.0
Gk3B2-05	45.6	0.073	6.4
Gk3B2-10	42.3	0.070	6.6
Gk3B2-20	36.3	0.067	7.4
Glauconite	41.2	0.056	5.4

3.4. Influence Nanocomposites on Plant Growth

The effect of glauconite-based nanofertilizers modified with zinc sulfate, copper chelate, and boric acid on the germination and growth of the oat (*Avena sativa*) was studied (Table 4). Germination energy did not show statistically significant differences from the control, although specific trends were observed. The highest germination energy (70%) was recorded for Gk3Zn2-05, while the lowest (55%) was noted for Gk3Zn2-20. Traditional fertilizers, such as zinc sulfate and copper chelate, showed slightly higher germination energy (71.2% and 70%, respectively) than nanocomposites, indicating their rapid nutrient availability.

Plant height and dry weight (biomass) varied among the nanocomposites (Table 4). The highest average plant height (15.5 ± 0.5 cm) was achieved in the Gk3Cu2-20 variant, exceeding the control by 7%. Similar results were observed for the nanocomposites Gk3B2-10, Gk3Cu2-10, and Gk3B2-20, with increases of 4.1%, 5.3%, and 6.2%, respectively. However,

copper chelate (15.9 ± 0.3 cm) and boric acid (15.6 ± 0.4 cm) demonstrated slightly greater increases in plant height, likely due to their immediate nutrient availability.

Table 4. Agrochemical parameters of the influence of nanocomposites on oat (*Avena sativa*) growth based on laboratory tests.

Samples	Germination Energy (%)	Plant Height (cm)	Dry Weight (g)
Gk3Zn2-20	70.0 ± 0.5	15.0 ± 0.4	0.247 ± 0.005
Gk3Zn2-10	66.0 ± 0.3	14.8 ± 0.2	0.244 ± 0.005
Gk3Zn2-05	55.0 ± 0.2	14.3 ± 0.3	0.220 ± 0.003
Gk3Cu2-20	66.0 ± 0.2	14.6 ± 0.3	0.240 ± 0.004
Gk3Cu2-10	69.0 ± 0.4	15.3 ± 0.6	0.245 ± 0.005
Gk3Cu2-05	64.0 ± 0.3	15.5 ± 0.2	0.238 ± 0.003
Gk3B2-20	63.0 ± 0.5	14.7 ± 0.3	0.242 ± 0.005
Gk3B2-10	63.9 ± 0.2	15.1 ± 0.5	0.243 ± 0.004
Gk3B2-05	64.7 ± 0.5	15.4 ± 0.3	0.246 ± 0.005
Control	62.0 ± 0.2	14.5 ± 0.3	0.231 ± 0.003
Glauconite	64.0 ± 0.2	14.9 ± 0.4	0.243 ± 0.005
Zinc sulfate	71.2 ± 0.3	15.2 ± 0.5	0.242 ± 0.005
Copper chelate	70.0 ± 0.2	15.9 ± 0.3	0.239 ± 0.004
Boric acid	67.0 ± 0.4	15.6 ± 0.4	0.243 ± 0.005

Values represent means ± standard deviations (n = 3). The statistical differences of variance components are indicated as $p < 0.05$.

The maximum dry weight was observed for Gk3Zn2-05, Gk3B2-20, and Gk3Cu2-10, with increases of 6.9%, 6.4%, and 5.9% compared to the control, respectively. Compared to the control, nanocomposites with Cu or B consistently showed increased plant height and dry weight. In contrast, the zinc-modified variants displayed mixed results, with Gk3Zn2-20 demonstrating growth parameters below the control. Nanocomposites consistently demonstrated comparable or slightly better performance than glauconite alone, highlighting their potential as improved fertilizers. For instance, zinc sulfate and boric acid provided a similar dry weight (0.242–0.243 g), but their faster nutrient release likely accounts for this efficiency.

4. Discussion

4.1. Mechanisms of Micronutrient Adsorption in Glauconite

Given the smaller Zn, Cu, and B ionic radius compared to the K and OH ions initially present in the glauconite structure, compression or stability of the layered crystalline structure is anticipated. Similar effects of layered structure compression have been observed for glauconite or interacting montmorillonite interacting with Cs^+ and K^+ or Ca^{2+} ions, respectively [36,37]. Molecular dynamics studies showed that increased layer charge promotes stronger inner-sphere coordination, which is also reflected in changes in interlayer thickness and pore structure compression [38–40]. The modification of glauconite with Zn^{2+} and Cu^{2+} ions enhances the layer charge of the mineral by partially replacing interlayer cations such as K^+ and Ca^{2+} with these strongly bound micronutrient ions. This increases the electrostatic attraction on the siloxane rings, promoting inner-sphere coordination and improving the retention capacity of the nanocomposites. This is confirmed by the fact that there is no significant expansion of the layered structure of glauconite when Zn or Cu ions enter the interlayer, compared to the intercalation of ammonium, for example [21,32]. Conversely, negatively charged boron (BO_3^-/BO_4^-) interacts predominantly with the outer-sphere coordination or basal edges of the crystalline structure, where residual positive charges compensate for its anionic nature. These differences in sorption mechanisms are critical for the efficiency of these fertilizers: Zn and Cu ions are released more slowly due to stronger binding, reducing leaching, while boron provides immediate nutrient availability by interacting with less tightly bound sites.

The chemical treatment of globular glauconite with zinc sulfate, copper chelate, and boric acid solutions induces specific structural changes while maintaining the stability of the mineral-layered matrix. Al-O-Si and O-Si-O deformation vibrations, Si-O and Al-O stretching vibrations, and OH vibrations (Figure 3) across all nanocomposites confirm the retention of the layered crystal structure despite the sorption of additional components. For zinc-modified nanocomposites, distinct peaks in the high-frequency region and weaker peaks in the mid-frequency region suggest interactions of Zn^{2+} with siloxane rings on the basal surface of glauconite, implying sorption via inner-sphere coordination. Trends in FTIR spectra indicate that higher Zn concentrations increase in the intensity of the 700 and 1120 cm^{-1} bands, highlighting concentration-dependent structural changes. Copper chelates induce localized changes in the mid-frequency region of the glauconite spectrum due to Cu-O stretching, also via inner-sphere coordination involving oxygen nodes. The FTIR spectra of boron-modified nanocomposites confirm vital peaks in the BO_4^- and BO_3^- regions, indicating the sorption of boron as outer-sphere complexes relative to the basal plane of glauconite. In numerous studies, the adsorption of metal ions on montmorillonite and kaolinite has been attributed to inner-sphere coordination, ensuring high sorption capacity and stability of interlayer bonds. For instance, Bhattacharyya and Gupta (2008) demonstrated that Cu^{2+} forms inner-sphere complexes on the basal surface of montmorillonite, leading to a significant increase in the thermodynamic stability of the structure [41]. Research on the adsorption of Zn^{2+} ions has shown that the smaller radii of these ions facilitate their efficient integration into the interlayer regions of clay minerals, including glauconite, montmorillonite, and beidellite [42].

The stability of potassium contents in the nanocomposites (Table 1) confirms that the sorption of Zn^{2+}, Cu^{2+}, and B occurs through interactions with interlayer water rather than via potassium cation substitution. This indicates the predominant role of exchange diffusion and inner- or outer-sphere coordination in the sorption processes. The results align with previous studies on micronutrient sorption in other layered silicates, such as smectites, kaolinites, and zeolites [36,43–45]. However, the unique globular morphology of glauconite, its high porosity, and significant iron content may enhance sorption kinetics and increase sorption capacity compared to similar materials. These properties make glauconite a promising material for nutrient delivery systems and sorption technologies [44,46,47].

Modifying glauconite with Zn, Cu, and B solutions significantly influences its thermal behavior (Figures 4 and 5). The observed endothermic and exothermic effects indicate changes in the energetics of crystal lattice dehydration and activation of interlayer interactions, particularly in Zn-modified nanocomposites. The exothermic effect in the 900–950 °C (Figure 4), absent in the original glauconite, highlights specific structural transformations in the nanocomposites. Six weight loss intervals, observed exclusively in Zn-modified samples, point to unique stages of dehydration and desorption. The release of SO^+ at high temperatures confirms the integration of zinc sulfates into the inner-sphere coordination on the basal surface of glauconite. This distinguishes Zn-modified nanocomposites from those modified by Cu and B, which exhibit less pronounced structural changes. Similar thermal effects associated with changes in dehydration and activation of interlayer interactions have previously been observed in mechanically activated kaolinite and montmorillonite, where additives contributed to structural stabilization and shifts in thermal characteristics [48,49]. The studied chemical activation of glauconite highlights the potential for targeted modification of the mineral's morphology and porosity while preserving its globular–lamellar structure. The increase in mesoporosity and surface area in Zn-modified nanocomposites confirms the material high sorption capacity. Similar changes in mesoporosity have been observed in studies on the activation of glauconite and smectites, where increased porosity enhanced sorption characteristics and the efficiency of slow nutrient release [32,50].

In Cu-modified nanocomposites, the presence of secondary phases, such as sulfates, on particle surfaces indicates the specific interaction of Cu^{2+} with the mineral. Modification with boric acid induces the localized restructuring of microparticles and pore channeling, which increases pore size and alters the mesoporous structure, albeit with a decrease in surface area. The effects of pore channeling have previously been reported in other clay minerals, such as halloysite nanotubes, leading to an increase in specific surface area and adsorption capacity [51,52]. This chemical activation provides a flexible approach to tailoring glauconite's structural and functional properties, enabling the creation of materials with optimized characteristics for specific applications.

Dynamic structural changes observed in Zn-modified nanocomposites, such as increased mesoporosity and specific surface area, indicate enhanced accessibility of active sorption sites. For Cu-modified nanocomposites, secondary phases on particle surfaces may stabilize the mineral structure while providing additional sorption sites. These structural and sorptive properties directly influence the efficiency of micronutrient delivery in soils. Strong inner-sphere binding of Zn and Cu ions ensures prolonged nutrient release, reducing leaching losses. Conversely, the rapid availability of boron ions from outer-sphere complexes is particularly beneficial for crops requiring immediate boron uptake.

4.2. Influence on Plant Growth and Future Directions

The agro-experiment results demonstrate the significant potential of glauconite modified with copper and boron to improve plant growth parameters. These variants consistently contributed to increased seedling length and biomass (Table 4), which can be attributed to the high availability of nutrients in the nanocomposites and their efficient uptake by plants. Particularly notable are the results for Gk3Cu2-20 and Gk3B2-20, which showed a maximum increase in seedling length by 7% and biomass by 6.4% compared to the control. Boric acid induces structural changes in glauconite pores, enhancing the release of BO_3^- and BO_4^- groups essential for plant growth. Similarly, secondary phases observed on the surface of copper-modified nanocomposites may facilitate prolonged and steady release of micronutrients. The results demonstrate that each nanocomposite group (Zn, Cu, and B) was applied independently, enabling comparisons within each micronutrient group. This ensured that the observed effects on plant growth were solely attributable to the specific sorption and release properties of each nanocomposite.

Glauconite modified with zinc exhibited mixed effects on growth parameters. The Gk3Zn2-05 variant improved germination rates to 100% and resulted in the highest dry biomass of seedlings, demonstrating its effectiveness at low dosages. However, the Gk3Zn2-20 variant showed reduced growth parameters due to the excessive concentration of zinc, which may have been toxic to plants. Recently, glauconite-based nanocomposites with macronutrients have demonstrated significant potential for improving plant growth due to their ability to release micronutrients [21,32]. Additionally, the chemical and thermal treatments of glauconite enhance its sorption properties, increasing nutrient availability for plants, which aligns with findings on the role of controlled-release materials in sustainable agriculture [53,54]. This highlights the need for the precise optimization of modifying agent dosages to minimize phytotoxicity. The findings emphasize the importance of developing flexible formulations of micronutrient nanocomposites based on glauconite, tailored to specific plant needs and growth conditions, to ensure maximum efficiency and sustainability in agricultural practices.

In addition to their direct use as fertilizers, glauconite nanocomposites have potential applications in soil remediation systems and as carriers for the slow release of other agrochemicals. Furthermore, these materials could be utilized in filtration systems to remove pollutants from agricultural runoff, making them valuable for addressing environ-

mental challenges and recycling. Glauconite's high sorption capacity and ion exchange properties make it a promising material for soil remediation, enabling the simultaneous passivation of contaminants and nutrient release [55]. This dual functionality is particularly valuable for reclaiming degraded soils and enhancing their fertility. Due to their high tetrahedral charge, glauconites are among the most effective sorbents for metals among layered aluminosilicates, attributed to complex sorption mechanisms involving not only ion exchange but also the presence of highly selective sorption sites on the lateral surfaces of glauconite [36]. These properties are particularly relevant in agriculture, where wastewater contamination can impact ecosystems and plant health [53,56]. Beyond wastewater treatment, nutrient-modified glauconites can be employed for the reclamation and regeneration of contaminated soils and landfills [57–60]. Due to their sorption activity and ion exchange capacity, glauconite nanocomposites can enrich soil with essential micro- and macronutrients while adsorbing heavy metals and radionuclides [61]. Expanding research to include their impact on soil microbiomes and long-term effectiveness will further establish their position as eco-friendly and efficient materials for agriculture and other environmentally significant applications [17].

5. Conclusions

The conducted study demonstrated the effectiveness of chemical activation of glauconite with Zn, Cu, and B solutions for creating multifunctional nanocomposites. The obtained results confirm the broad potential of modified materials in terms of sorption, structural properties, and agrochemical effects.

1. The chemical activation of glauconite with Zn, Cu, and B solutions preserves its primary globular–lamellar morphology. This confirms the mineral's morphological and structural stability and suitability for further modification to create multifunctional materials.
2. The modification of glauconite significantly enhances its sorption properties due to effective interlayer diffusion, inner-sphere coordination of Zn^{2+} and Cu^{2+} ions, and outer-sphere coordination of BO_3^-/BO_4^-. This enables the regulation of sorption parameters for targeted micronutrient release.
3. Nanocomposites with zinc demonstrated an increase in specific surface area (up to 50 m^2/g) and mesopore volume, attributed to their active ion exchange capacity. In contrast, boric acid modification led to increased pore diameter (up to 7.4 nm) and a reduction in specific surface area due to local structural rearrangements and pore channeling.
4. Using nanocomposites with copper and boron improved plant growth parameters, including a 7% increase in seedling length and a 6.4% increase in biomass compared to the control. Zinc-modified variants demonstrated effectiveness at low dosages but reduced growth at high concentrations, emphasizing the importance of optimizing initial solution dosages.
5. The findings underscore the potential for targeted modifications of glauconite's morphological and functional properties. This paves the way for developing customizable nanocomposites designed for specific purposes, such as improving agrochemical properties or adapting to various soil conditions.

Author Contributions: Conceptualization, M.R.; methodology, M.R., I.K., P.B., A.R. and P.M.; software, N.M., K.I. and K.P.; validation, P.B.; formal analysis, M.R., I.K. and A.R.; investigation, I.K., P.M., E.D., K.I., K.P., N.M. and M.R.; resources, M.R.; data curation, M.R.; writing—original draft preparation, M.R. and I.K.; writing—review and editing, M.R., I.K., E.D. and P.B.; visualization, I.K.,

P.M., E.D., K.I., K.P., N.M. and M.R.; supervision, M.R.; project administration, M.R. and A.R.; funding acquisition, M.R. All authors have read and agreed to the published version of the manuscript.

Funding: The authors gratefully acknowledge the financial support provided by the Russian Science Foundation through the research project N° 22-77-10002.

Data Availability Statement: Data are contained within the article.

Acknowledgments: A.R. acknowledges the project FSWW-2023-0010. The authors thank three anonymous reviewers and the editor for their insightful feedback, which significantly improved the clarity and quality of the manuscript.

Conflicts of Interest: The authors declare no conflicts of interest.

References

1. Jariwala, H.; Santos, R.M.; Lauzon, J.D.; Dutta, A.; Wai Chiang, Y. Controlled Release Fertilizers (CRFs) for Climate-Smart Agriculture Practices: A Comprehensive Review on Release Mechanism, Materials, Methods of Preparation, and Effect on Environmental Parameters. *Environ. Sci. Pollut. Res.* **2022**, *2022*, 53967–53995. [CrossRef]
2. Sharma, G.C. Controlled-Release Fertilizers and Horticultural Applications. *Sci. Hortic.* **1979**, *11*, 107–129. [CrossRef]
3. Trenkel, M.E. *Controlled-Release and Stabilized Fertilizers in Agriculture*; International Fertilizer Industry Association: Paris, France, 1997.
4. Govil, S.; Van Duc Long, N.; Escribà-Gelonch, M.; Hessel, V. Controlled-Release Fertiliser: Recent Developments and Perspectives. *Ind. Crops Prod.* **2024**, *219*, 119160. [CrossRef]
5. Trenkel, M.E. *Slow- and Controlled-Release and Stabilized Fertilizers: An Option for Enhancing Nutrient Use Efficiency in Agriculture*; International Fertilizer Industry Association (IFA): Paris, France, 2010; ISBN 9788578110796.
6. Ni, B.; Liu, M.; Lü, S.; Xie, L.; Wang, Y. Environmentally Friendly Slow-Release Nitrogen Fertilizer. *J. Agric. Food Chem.* **2011**, *59*, 10169–10175. [CrossRef]
7. Chen, L.; Chen, X.L.; Zhou, C.H.; Yang, H.M.; Ji, S.F.; Tong, D.S.; Zhong, Z.K.; Yu, W.H.; Chu, M.Q. Environmental-Friendly Montmorillonite-Biochar Composites: Facile Production and Tunable Adsorption-Release of Ammonium and Phosphate. *J. Clean. Prod.* **2017**, *156*, 648–659. [CrossRef]
8. Obieze, C.C.; Chikere, C.B.; Adeleke, R.; Akaranta, O. Formulation and Evaluation of Slow-Release Fertilizer from Agricultural and Industrial Wastes for Remediation of Crude Oil-Polluted Soils. In Proceedings of the Society of Petroleum Engineers—SPE Nigeria Annual International Conference and Exhibition 2019, NAIC 2019, Lagos, Nigeria, 5–7 August 2019. [CrossRef]
9. Akiyama, H.; Yan, X.; Yagi, K. Evaluation of Effectiveness of Enhanced-Efficiency Fertilizers as Mitigation Options for N2O and NO Emissions from Agricultural Soils: Meta-Analysis. *Glob. Change Biol.* **2010**, *16*, 1837–1846. [CrossRef]
10. IPCC. *IPCC Climate Change 2014: Mitigation of Climate Change: Working Group III Contribution to the Fifth Assessment Report of the Intergovernmental Panel on Climate Change 2014*; IPCC: Geneva, Switzerland, 2014.
11. Liu, Q.; Liu, Y.; Hao, X.; Song, C.; Zong, Y.; Zhang, D.; Shi, X.; Li, P. Effects of Controlled-Release Fertilizer on N2O Emissions in Wheat under Elevated CO2 Concentration and Temperature. *Plant Soil* **2023**, *3*, 343–361. [CrossRef]
12. Pretty, J.; Sutherland, W.J.; Ashby, J.; Auburn, J.; Baulcombe, D.; Bell, M.; Bentley, J.; Bickersteth, S.; Brown, K.; Burke, J.; et al. The Top 100 Questions of Importance to the Future of Global Agriculture. *Int. J. Agric. Sustain.* **2010**, *8*, 219–236. [CrossRef]
13. Tilman, D.; Cassman, K.G.; Matson, P.A.; Naylor, R.; Polasky, S. Agricultural Sustainability and Intensive Production Practices. *Nature* **2002**, *418*, 671–677. [CrossRef]
14. Easwaran, C.; Christopher, S.R.; Moorthy, G.; Mohan, P.; Marimuthu, R.; Koothan, V.; Nallusamy, S. Nano Hybrid Fertilizers: A Review on the State of the Art in Sustainable Agriculture. *Sci. Total Environ.* **2024**, *929*, 172533. [CrossRef] [PubMed]
15. Zhang, X.-M.; Hu, C.; He, Z.-Q.; Abbas, Y.; Li, Y.; Lv, L.-F.; Hao, X.-Y.; Gai, G.-S.; Huang, Z.-H.; Yang, Y.-F.; et al. Microcrystalline Apatite Minerals: Mechanochemical Activation for Agricultural Application. *Minerals* **2019**, *9*, 211. [CrossRef]
16. Leite, A.d.A.; de Resende, I.A.D.; Lago, B.C.; Barrera, A.M.V.; Montes, A.O.; de Assis Pereira, T.; Dourado Leal Queiroz, D.; Melo, L.C.A. Increasing the Fertilizer Efficiency of Potassium Silicate by Co-Pyrolysis and Chemical Activation. *J. Soil Sci. Plant Nutr.* **2024**, *24*, 2249–2262. [CrossRef]
17. Dasi, E.; Rudmin, M.; Banerjee, S. Glauconite Applications in Agriculture: A Review of Recent Advances. *Appl. Clay Sci.* **2024**, *253*, 107368. [CrossRef]
18. Puspita, A.; Pratiwi, G.; Fatimah, I. Chitosan-Modified Smectite Clay and Study on Adsorption-Desorption of Urea. *Chem. Eng. Trans.* **2017**, *56*, 1645–1650. [CrossRef]
19. Sharma, N.; Singh, A.; Dutta, R.K. Biodegradable Fertilizer Nanocomposite Hydrogel Based on Poly(Vinyl Alcohol)/Kaolin/Diammonium Hydrogen Phosphate (DAhP) for Controlled Release of Phosphate. *Polym. Bull.* **2021**, *78*, 2933–2950. [CrossRef]

20. Borges, R.; Baika, L.M.; Grassi, M.T.; Wypych, F. Mechanochemical Conversion of Chrysotile/K2HPO4 Mixtures into Potential Sustainable and Environmentally Friendly Slow-Release Fertilizers. *J. Environ. Manag.* **2018**, *206*, 962–970. [CrossRef] [PubMed]
21. Rudmin, M.; Banerjee, S.; Makarov, B.; Belousov, P.; Kurovsky, A.; Ibraeva, K.; Buyakov, A. Glauconite-Urea Nanocomposites As Polyfunctional Controlled-Release Fertilizers. *J. Soil Sci. Plant Nutr.* **2022**, *22*, 4035–4046. [CrossRef]
22. Rudmin, M.; Banerjee, S.; Yakich, T.; Tabakaev, R.; Ibraeva, K.; Buyakov, A.; Soktoev, B.; Ruban, A. Formulation of a Slow-Release Fertilizer by Mechanical Activation of Smectite/Glauconite and Urea Mixtures. *Appl. Clay Sci.* **2020**, *196*, 105775. [CrossRef]
23. Bailey, S.W. Summary of Recommendations of AIPEA Nomenclature Committee on Clay Minerals. *Am. Mineral.* **1980**, *65*, 1–7. [CrossRef]
24. Guggenheim, S.; Adams, J.M.; Bain, D.C.; Bergaya, F.; Brigatti, M.F.; Drits, V.A.; Formoso, M.L.L.; Galan, E.; Kogure, T.; Stanjek, H. Summary of Recommendations of Nomenclature Committees Relevant to Clay Mineralogy: Report of the Association International Pour l'Etude Des Argiles (AIPEA) Nomenclature Committee for 2006 (Clays and Clay Minerals). *Clays Clay Miner.* **2007**, *55*, 761–772. [CrossRef]
25. Drits, V.A. Isomorphous Cation Distribution in Celadonites, Glauconites and Fe-Illites Determined by Infrared, Mössbauer and EXAFS Spectroscopies. *Clay Miner.* **1997**, *32*, 153–179. [CrossRef]
26. Drits, V.A.; Ivanovskaya, T.A.; Sakharov, B.A.; Zvyagina, B.B.; Derkowski, A.; Gor'kova, N.V.; Pokrovskaya, E.V.; Savichev, A.T.; Zaitseva, T.S. Nature of the Structural and Crystal-Chemical Heterogeneity of the Mg-Rich Glauconite (Riphean, Anabar Uplift). *Lithol. Miner. Resour.* **2010**, *45*, 555–576. [CrossRef]
27. Odom, I.E. 13. GLAUCONITE and CELADONITE MINERALS. In *Micas*; Bailey, S.W., Ed.; De Gruyter: Berlin, Germany, 1984; Volume 13, pp. 545–572. ISBN 9781501508820.
28. Rieder, M.; Cavazzini, G.; D'yakonov, Y.S.; Frank-Kamenetskii, V.A.; Gottardi, G.; Guggenheim, S.; Koval', P.V.; Müller, G.; Neiva, A.M.R.; Radoslovich, E.W.; et al. Nomenclature of the Micas. *Can. Mineral.* **1988**, *36*, 905–912.
29. Lenaz, D.; Giovanoni, S.; Parrino, F.; Bersani, D.; Parisi, F. Maturation Stages of Glauconites: A Combined Electron Microprobe, Raman, and Thermogravimetric Study. *Ceram. Int.* **2022**, *49*, 14927–14933. [CrossRef]
30. Ivanovskaya, T.A.; Zviagina, B.B.; Zaitseva, T.S. Secondary Alterations of Globular and Platy Phyllosilicates of the Glauconite–Illite Series in the Precambrian and Vendian–Cambrian Rocks. *Lithol. Miner. Resour.* **2017**, *52*, 369–391. [CrossRef]
31. Ivanovskaya, T.A.; Sakharov, B.A.; Zaitseva, T.S. Globular Phyllosilicates of the Glauconite–Illite Series in the Cambrian and Ordovician Rocks of the Eastern Baltica (Northern Estonia, Western Lithuania, and Western Latvia). *Lithol. Miner. Resour.* **2023**, *58*, 158–176. [CrossRef]
32. Rudmin, M.; Maximov, P.; Dasi, E.; Kurovsky, A.; Gummer, Y.; Ibraeva, K.; Kutugin, V.; Soktoev, B.; Ponomarev, K.; Tararushkin, E.; et al. Intercalation of Carbamide to Globular Glauconite by Chemical Processing for the Creation of Slow-Release Nanocomposites. *Appl. Clay Sci.* **2023**, *243*, 107075. [CrossRef]
33. Singla, R.; Alex, T.C.; Kumar, R. On Mechanical Activation of Glauconite: Physicochemical Changes, Alterations in Cation Exchange Capacity and Mechanisms. *Powder Technol.* **2020**, *360*, 337–351. [CrossRef]
34. Terentyev, Y.N.; Syrchina, N.V.; Ashikhmina, T.Y.; Kantor, G.Y. Natural sulfur fertilizer with activated peat and glauconitic efel. *Theor. Appl. Ecol.* **2019**, *2019*, 134–141. [CrossRef]
35. Rudmin, M.; Mazurov, A.; Banerjee, S. Origin of Ooidal Ironstones in Relation to Warming Events: Cretaceous-Eocene Bakchar Deposit, South-East Western Siberia. *Mar. Pet. Geol.* **2019**, *100*, 309–325. [CrossRef]
36. Belousov, P.; Semenkova, A.; Egorova, T.; Romanchuk, A.; Zakusin, S.; Dorzhieva, O.; Tyupina, E.; Izosimova, Y.; Tolpeshta, I.; Chernov, M.; et al. Cesium Sorption and Desorption on Glauconite, Bentonite, Zeolite and Diatomite. *Minerals* **2019**, *9*, 625. [CrossRef]
37. Bruneel, Y.; Van Laer, L.; Brassinnes, S.; Smolders, E. Characterisation of the Highly Selective Caesium Sorption on Glauconite Rich Sands of Contrasting Geological Formations. *Appl. Geochem.* **2021**, *128*, 104926. [CrossRef]
38. Peng, C.; Wang, G.; Zhu, X.; Qin, L.; Shao, X. Adsorption of Ammonium Ions onto the External Surface of Smectite: Effects of Layer Charge, Concentration, Anion and Comparison with Interlayer Adsorption. *Appl. Clay Sci.* **2022**, *230*, 106716. [CrossRef]
39. Peng, C.; Wang, G.; Qin, L.; Luo, S.; Min, F.; Zhu, X. Molecular Dynamics Simulation of NH4-Montmorillonite Interlayer Hydration: Structure, Energetics, and Dynamics. *Appl. Clay Sci.* **2020**, *195*, 105657. [CrossRef]
40. Hatami, H.; Fotovat, A.; Halajnia, A. Comparison of Adsorption and Desorption of Phosphate on Synthesized Zn-Al LDH by Two Methods in a Simulated Soil Solution. *Appl. Clay Sci.* **2018**, *152*, 333–341. [CrossRef]
41. Bhattacharyya, K.G.; Gupta, S. Sen Adsorption of a Few Heavy Metals on Natural and Modified Kaolinite and Montmorillonite: A Review. *Adv. Colloid Interface Sci.* **2008**, *140*, 114–131. [CrossRef]
42. Brigatti, M.F.; Galan, E.; Theng, B.K.G. Chapter 2 Structures and Mineralogy of Clay Minerals. In *Developments in Clay Science*; Elsevier: Amsterdam, The Netherlands, 2006; Volume 1, pp. 19–86.
43. Ismael, I.S.; Kharbish, S. Removing of As(V) from Aqueous Solution Using Natural and Pretreated Glauconite and Halloysite. *Carpathian J. Earth Environ. Sci.* **2013**, *8*, 187–198.

44. Selim, K.A.; El-Tawil, R.S.; Rostom, M. Utilization of Surface Modified Phyllosilicate Mineral for Heavy Metals Removal from Aqueous Solutions. *Egypt. J. Pet.* **2018**, *27*, 393–401. [CrossRef]
45. Allah, A.F.; Shaban, M.; Alqhtani, H.A.; Bin-Jumah, M.; Alenazi, N.A.; Allam, A.A.; Abukhadra, M.R. Effective Remediation of Toxic Metal Ions (Cd(II), Pb(II), Hg(II), and Ba(II)) Using Mesoporous Glauconite-Based Iron Silicate Nanorods: Experimental and Theoretical Studies. *Microporous Mesoporous Mater.* **2025**, *382*, 113390. [CrossRef]
46. Belousov, P.E.; Gorbunova, E.M.; Kim, K.B.; Niftaliev, S.I.; Krupskaya, V.V.; Rudmin, M.A.; Koroleva, T.A.; Rumyantseva, A.O. Magnetic and Hydrophobic Sorbent Based on Glauconite for the Removal of Oil Slick from the Water Surface. *Int. J. Environ. Sci. Technol.* **2024**, 1–12. [CrossRef]
47. Semenkova, A.; Belousov, P.; Rzhevskaia, A.; Izosimova, Y.; Maslakov, K.; Tolpeshta, I.; Romanchuk, A.; Krupskaya, V. U(VI) Sorption onto Natural Sorbents. *J. Radioanal. Nucl. Chem.* **2020**, *326*, 293–301. [CrossRef]
48. Borges, R.; Brunatto, S.F.; Leitão, A.A.; De Carvalho, G.S.G.; Wypych, F. Solid-State Mechanochemical Activation of Clay Minerals and Soluble Phosphate Mixtures to Obtain Slow-Release Fertilizers. *Clay Miner.* **2015**, *50*, 153–162. [CrossRef]
49. Mañosa, J.; la Rosa, J.C.; Silvello, A.; Maldonado-Alameda, A.; Chimenos, J.M. Kaolinite Structural Modifications Induced by Mechanical Activation. *Appl. Clay Sci.* **2023**, *238*, 106918. [CrossRef]
50. Baldermann, A.; Landler, A.; Mittermayr, F.; Letofsky-Papst, I.; Steindl, F.; Galan, I.; Dietzel, M. Removal of Heavy Metals (Co, Cr, and Zn) during Calcium–Aluminium–Silicate–Hydrate and Trioctahedral Smectite Formation. *J. Mater. Sci.* **2019**, *54*, 9331–9351. [CrossRef]
51. Kang, M.; Lin, W.; Liang, C.; Zeng, J.; Wang, Y.; Guan, Y.; Cheng, J. Construction of Ammonium Polyphosphate-Modified Halloysite Nanotubes on Phase Change Material Microcapsules for the Enhancement of Thermophysical Performance and Flame Retardant Properties. *Appl. Therm. Eng.* **2024**, *239*, 122160. [CrossRef]
52. Fahimizadeh, M.; Wong, L.W.; Baifa, Z.; Sadjadi, S.; Auckloo, S.A.B.; Palaniandy, K.; Pasbakhsh, P.; Tan, J.B.L.; Singh, R.K.R.; Yuan, P. Halloysite Clay Nanotubes: Innovative Applications by Smart Systems. *Appl. Clay Sci.* **2024**, *251*, 107319. [CrossRef]
53. Rahman, M.H.; Haque, K.M.S.; Khan, M.Z.H. A Review on Application of Controlled Released Fertilizers Influencing the Sustainable Agricultural Production: A Cleaner Production Process. *Environ. Technol. Innov.* **2021**, *23*, 101697. [CrossRef]
54. Basak, B.B. Waste Mica as Alternative Source of Plant-Available Potassium: Evaluation of Agronomic Potential Through Chemical and Biological Methods. *Nat. Resour. Res.* **2018**, *28*, 953–965. [CrossRef]
55. Xia, L.; Verbeeck, M.; Bergen, B.; Smolders, E. Effect of External and Internal Loading on Source-Sink Phosphorus Dynamics of River Sediment Amended with Iron-Rich Glauconite Sand. *J. Environ. Manag.* **2023**, *332*, 117396. [CrossRef] [PubMed]
56. Liu, J.; Yang, Y.; Gao, B.; Li, Y.C.; Xie, J. Bio-Based Elastic Polyurethane for Controlled-Release Urea Fertilizer: Fabrication, Properties, Swelling and Nitrogen Release Characteristics. *J. Clean. Prod.* **2019**, *209*, 528–537. [CrossRef]
57. Mobarak, M.; Salah, A.M.; Selim, A.Q.; Al-Arifi, N.; Salama, Y.F.; Li, Z.; Seliem, M.K. Magnetic Hybrid Spheres of Glauconite/Calcium Alginate Interface for Methylene Blue Adsorption: Synthesis, Characterization, and Novel Physicochemical Insights through Theoretical Treatment. *Int. J. Biol. Macromol.* **2024**, *277*, 134106. [CrossRef]
58. Chayka, O.; Petrushka, I.; Ruda, M.; Paranyak, N.; Matskiv, O. The Minimization of Impact of Oil Pollution on Soils in the Area of Railways Using Glauconite. *J. Water Land Dev.* **2021**, *49*, 79–84. [CrossRef]
59. Khopyak, N.; Tkachenko, H.; Manenko, A. Neutralization of Oil Spills Using Ecological Sorbent Glauconite Modified by Biosurfactants of Pseudomonas Spp. Ps-17. *J. Ecol. Prot. Coastline* **2016**, *19*, 49–66.
60. Chukaeva, M.; Zaytseva, T.; Matveeva, V.; Sverchkov, I. Purification of Oil-Contaminated Wastewater with a Modified Natural Adsorbent. *Ecol. Eng. Environ. Technol.* **2021**, *22*, 46–51. [CrossRef]
61. Voronina, A.V.; Noskova, A.Y.; Semenishchev, V.S.; Gupta, D.K. Decontamination of Seawater from 137Cs and 90Sr Radionuclides Using Inorganic Sorbents. *J. Environ. Radioact.* **2020**, *217*, 106210. [CrossRef] [PubMed]